forests

MDPI

Article

Integrated Extraction of Root Diameter and Location in Ground-Penetrating Radar Images via CycleGAN-Guided Multi-Task Neural Network

Xihong Cui [1], Shupeng Li [2], Luyun Zhang [3], Longkang Peng [4], Li Guo [5], Xin Cao [1], Xuehong Chen [1], Huaxiang Yin [3] and Miaogen Shen [1,*]

[1] State Key Laboratory of Remote Sensing Science, Faculty of Geographical Science, Beijing Normal University, Beijing 100875, China; cuixihong@bnu.edu.cn (X.C.); caoxin@bnu.edu.cn (X.C.); chenxuehong@bnu.edu.cn (X.C.)
[2] Big Data Center of Ministry of Emergency Management, Beijing 100013, China; shupeng_lee@163.com
[3] Academy of Remote Sensing Science and Engineering, Faculty of Geographical Science, Beijing Normal University, Beijing 100875, China; luyun@mail.bnu.edu.cn (L.Z.); yinhuaxiang@mail.bnu.edu.cn (H.Y.)
[4] Department of Land Surveying and Geo-Informatics, The Hong Kong Polytechnic University, Hong Kong, China; longkang.peng@connect.polyu.hk
[5] State Key Laboratory of Hydraulics and Mountain River Engineering, College of Water Resource and Hydropower, Sichuan University, Chengdu 610065, China; liguo01@scu.edu.cn
* Correspondence: shenmiaogen@bnu.edu.cn

Abstract: The diameter of roots is pivotal for studying subsurface root structure geometry. Yet, directly obtaining these parameters is challenging due their hidden nature. Ground-penetrating radar (GPR) offers a reproducible, nondestructive method for root detection, but estimating diameter from B-Scan images remains challenging. To address this, we developed the CycleGAN-guided multi-task neural network (CMT-Net). It comprises two subnetworks, YOLOv4-Hyperbolic Position and Diameter (YOLOv4-HPD) and CycleGAN. The YOLOv4-HPD is obtained by adding a regression header for predicting root diameter to YOLOv4-Hyperbola, which achieves the ability to simultaneously accurately locate root objects and estimate root diameter. The CycleGAN is used to solve the problem of the lack of a real root diameter training dataset for the YOLOv4-HPD model by migrating field-measured data domains to simulated data without altering root diameter information. We used simulated and field data to evaluate the model, showing its effectiveness in estimating root diameter. This study marks the first construction of a deep learning model for fully automatic root location and diameter extraction from GPR images, achieving an "Image Input–Parameter Output" end-to-end pattern. The model's validation across various dataset scales opens the way for estimating other root attributes.

Keywords: root diameter; ground-penetrating radar; deep learning; root location

check for updates

Academic Editor: Jan Bocianowski

Received: 6 December 2024
Revised: 24 December 2024
Accepted: 9 January 2025
Published: 9 January 2025

Citation: Cui, X.; Li, S.; Zhang, L.; Peng, L.; Guo, L.; Cao, X.; Chen, X.; Yin, H.; Shen, M. Integrated Extraction of Root Diameter and Location in Ground-Penetrating Radar Images via CycleGAN-Guided Multi-Task Neural Network. *Forests* **2025**, *16*, 110. https://doi.org/10.3390/f16010110

Copyright: © 2025 by the authors. Licensee MDPI, Basel, Switzerland. This article is an open access article distributed under the terms and conditions of the Creative Commons Attribution (CC BY) license (https://creativecommons.org/licenses/by/4.0/).

1. Introduction

Plant roots play a key role in plant function and performance [1], and they enhance the adaptability to the subsurface soil environment by adjusting root size, root biomass, and root length [2]. Root diameter is one of the important parameters in measuring the characteristics of an underground root system. [3,4]. However, obtaining root diameter information under field conditions is difficult because field investigations are often destructive, laborious, and time-consuming [5–7]. GPR has been successfully used as a non-destructive tool to detect plant roots and estimate their diameter parameters [3,8].

The principle of GPR to detect plant roots is that due to the difference between the dielectric constant of the root and the surrounding soil, the electromagnetic waves emitted by GPR are reflected when they hit the root as they travel through the soil, and the interpretation of the reflected EM signal provides the relevant attribute information of the root [9]. Some studies have attempted to estimate root diameters using A-Scan data from GPR, requiring a multiple regression model between waveform parameters of the A-Scan passing through the center of each root and the root diameter [3,5,10]. However, the accuracy of such models varies widely due to inconsistencies in waveform parameter selection and A-Scan extraction [5,8,11]. Several studies were based on hyperbolic features in GPR B-scan images [12–15]. Such methods require merging the raw GPR data into a mathematical model of hyperbolic reflections and then estimating the root diameter by fitting the hyperbolic curves. The common fitting methods are least-squares fitting [14] and recursive Kalman filtering [16]. However, the shape of the hyperbola is not sensitive to the diameter information, and it is difficult to estimate the diameter of the subsurface root accurately.

In recent years, deep learning algorithms have been used to identify root objects and estimate root diameters. Sun H. H. et al. proposed a multi-polarimetric integration neural network (MMI-Net) for simultaneously estimating multiple root-related parameters in heterogeneous soil environments [17]. Sun D. et al. used YOLOv5s to automatically detect root objects in B-scan images of GPR, and then estimated root diameter by the three-point fixed circle (TPFC) method [15]. Hao Liang et al. proposed a back propagation neural network model for root diameter estimation [18]. These studies show more stable prediction results than regression models, demonstrating the superiority of deep learning algorithms in root target detection and related parameter extraction [18]. However, these approaches mostly rely on simulation experiments and lack validation with real root systems and heterogeneous soils.

In summary, estimating root diameter from GPR data using deep learning models faces several challenges. Firstly, data acquisition is difficult since root diameter information cannot be directly measured in field conditions. Traditional GPR methods fail to provide explicit diameter data, resulting in insufficient support for training deep learning models. Secondly, data annotation is problematic, as precise labeling of root diameters in GPR images is time-consuming and error-prone, complicating the construction of high-quality training datasets. Thirdly, existing datasets often lack diversity, limiting model generalization across varying soil conditions and root types. Lastly, image quality is affected by underground soil heterogeneity, including variations in moisture, which increase noise and reduce extraction accuracy. In addition, in the existing research [15,17,18], accurate localization of root objects is required before extracting root diameters; these are two independent data processing operations that are cumbersome to operate. There is an urgent need to construct a model that can unify the two for fully automated "end-to-end" extraction of root diameters.

To address these issues, this study proposes the CMT-Net model, which effectively overcomes these challenges through several key strategies. First, data simulation and domain adaptation methods are employed [19–21]. Simulated data with various root diameters are generated using the professional simulation software gprMax, and a CycleGAN is utilized for domain adaptation [22], transforming simulated data into training data with realistic soil backgrounds and precise root diameter labels, thus mitigating data acquisition difficulties. Second, CMT-Net incorporates a multi-task learning framework. The integrated YOLOv4-HPD subnetwork simultaneously performs root target detection and diameter estimation, providing an automated end-to-end processing workflow that reduces reliance on manual labeling. Third, leveraging the feature extraction capabilities of deep

convolutional neural networks (DCNN) [23–25], the model extracts rich root characteristics from GPR images and models their relationship with root diameter, enhancing applicability and robustness under diverse soil conditions. Finally, the use of an L1 loss function in model optimization improves diameter regression stability and minimizes the impact of outliers on performance. The CMT-Net model enhances automation in root localization and diameter estimation while addressing challenges in data acquisition, feature extraction, and model robustness.

This article's outline is as follows: The Introduction section discusses the significance of root diameter in studying underground root systems, highlights the challenges of directly acquiring root diameter data, and outlines how CMT-Net effectively addresses these issues by integrating deep learning and data migration techniques. The Materials and Methods section provides a detailed explanation of the CMT-Net architecture, including the pivotal role of the CycleGAN subnetwork in data migration and the functionality of the YOLOv4-HPD subnetwork in root position detection and diameter estimation. This section also elaborates on the experimental setup, dataset construction process, and principles for selecting evaluation metrics. The Results section demonstrates the model's performance on both simulated and real-world data, validating the robustness and effectiveness of CMT-Net across various complex environments. The Discussion section analyzes the model's advantages in terms of accuracy and applicability, offers a comprehensive comparison with existing methods, and summarizes the potential application scenarios of CMT-Net, such as agriculture, forestry, and environmental monitoring. Additionally, the paper identifies limitations in data diversity and three-dimensional structure analysis, providing direction for future research.

2. Materials and Methods

2.1. CMT-Net Model

This study presents a CycleGAN-guided multi-task neural network (CMT-Net) model that is capable of detecting subsurface root objects and extracting root diameters under varying soil conditions. The overall network structure of CMT-Net comprises two subnetworks (shown in Figure 1): CycleGAN and YOLOv4-HPD (YOLOv4-Hyperbolic Position and Diameter). CycleGAN is used for domain migration to generate the diameter training dataset of roots with complex backgrounds in the field. YOLOv4-HPD is proposed based on YOLOv4 and improved for the YOLOv4-Hyperbola model [19] by further expanding the prediction head so that it can estimate the root diameter simultaneously on the foundation of the predicted position. The integrated framework of CMT-Net offers a comprehensive solution for accurate root diameter estimation from GPR images in real-world scenarios.

2.1.1. CycleGAN

The GPR cannot obtain the root diameter information directly when measuring the plant root system, so it is not possible to construct a training dataset with real root diameter information. However, it is possible to simulate the root system dataset with root diameter and other attributes through the professional simulation software GprMax. Therefore, we can migrate it to the GPR real measurement dataset through the domain adaptation model. CycleGAN is just right for the purpose of training on the simulated data and then applying it to the measured data [22]. There are two reasons for choosing CycleGAN in this study.

(a) Prior to CycleGAN, domain adaptation models such as Pix2Pix [26] required paired training data, consisting of identical image content with different styles. However, due to the complexity of underground root growth conditions and the diverse characteristics of GPR images, simulating corresponding images one by one is impossible. CycleGAN

addresses this challenge by using data from only two domains, which do not need to have a strict correspondence, and can still be used at the ensemble level for supervised learning.

(b) Our purpose is to migrate only the root diameter information from the simulated data to the real measurement image, to obtain a dataset with both the background of the real data and the diameter attribute of the root. This enables the simulated dataset to be close enough to the actual measurement environment, thereby ensuring that the model can accurately learn the diameter feature of the root on the image. CycleGAN is able to achieve this purpose very well.

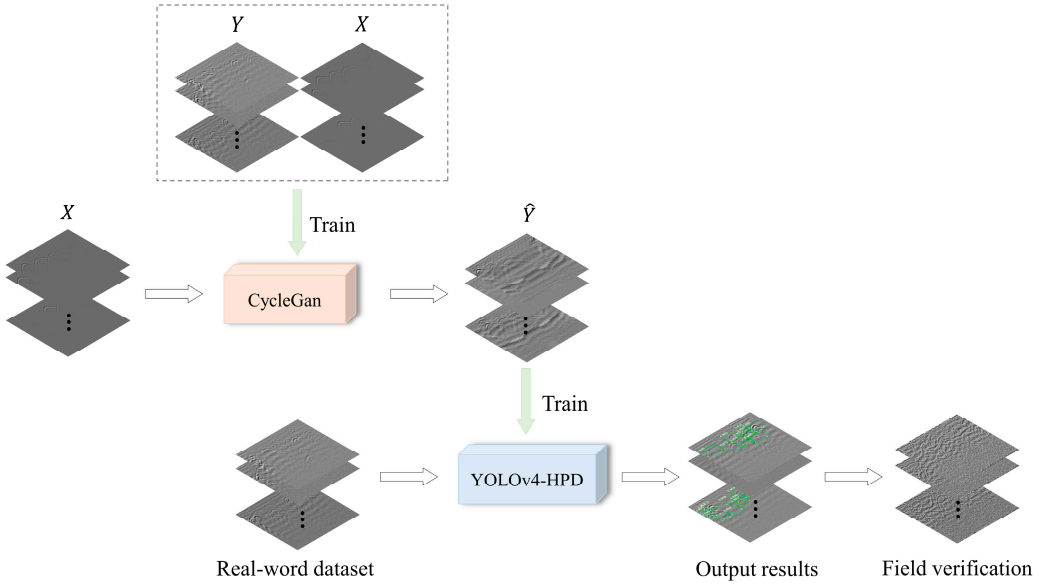


Figure 1. The overall framework of CMT-Net: X is the source domain dataset with an attribute label, Y is the target domain dataset without an attribute label, and Ŷ is the image generated by the CycleGAN generator.

CycleGAN is a ring network consisting of two mirror-symmetric Generative Adversarial Networks (GANs), each having two generators and two discriminators. The network is divided into a forward network (source domain X to target domain Y) and a reverse network (target domain Y to source domain X). The loss function of CycleGAN comprises two parts: generative adversarial loss and cycle-consistency loss. The generative adversarial loss ensures that the mapped data distribution is similar to that of the target domain, making the generator produce more realistic images. Taking the forward network (shown in Figure 2) as an example, the generator G maps the image from the source domain X to the target domain space, and obtains the output $\hat{Y}$ with the same distribution as the target domain Y. The discriminator D_Y determines whether $\hat{Y}$ is the real image and then reduces it to the data $\hat{X}$ in the source domain by the generator F.

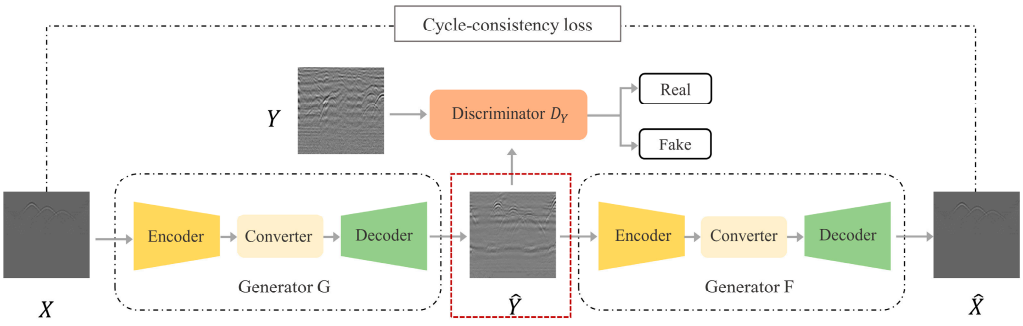


Figure 2. CycleGAN forward network structure.

The loss functions of generator G: $X \rightarrow Y$ and discriminator D_Y are defined as shown in Equation (1). The reverse network is the same process as above, and the loss functions of generator F: $Y \rightarrow X$ and discriminator D_X are defined as shown in Equation (2). The generator aims to minimize the loss function value, while the discriminator aims to maximize the loss function value, and this study is more concerned with the performance of the generator G and the discriminator D_Y.

$$E_{x \sim P_{data(x)}}[log(1 - D_Y(G(x)))], \tag{1}$$

$$L_{GAN}(F, D_X, Y, X) = E_{x \sim P_{data(x)}}[logD_X(x)] + E_{y \sim P_{data(y)}}[log(1 - D_X(F(y)))], \tag{2}$$

where X, Y represent the source domain and target domain, $x \in X$, $y \in Y$, $P_{data(x)}$ is the data distribution of the source domain dataset, $P_{data(y)}$ is the data distribution of the target domain dataset, $\sim$ denotes the obedience relation, and E is the mathematical expectation function.

Cycle-consistency loss serves to make the learned two generators G and F not contradict each other, ensuring that the output image of the generator is only different in style from the input image, and the content is the same. For each image x from the source domain, the original image can be regenerated after one cycle: $x \rightarrow G(x) \rightarrow F(G(x)) \approx x$, which can be called forward cycle consistency. The reverse cycle consistency is $y \rightarrow F(y) \rightarrow G(F(y)) \approx y$. It calculates the loss between $F(G(x))$ $(G(F(y)))$ and $x(y)$ by introducing the cycle-consistency loss function (as in Equation (3)).

$$L_{cyc}(G, F) = E_{x \sim P_{data(x)}}[\| F(G(x)) - x \|_1] + E_{y \sim P_{data(y)}}[\| G(F(y)) - y \|_1] \tag{3}$$

Thus the total loss function of CycleGAN is as in Equation (4), where λ is the weight factor of the cycle-consistency loss function:

$$Loss = L_{GAN}(G, D_Y, X, Y) + L_{GAN}(F, D_X, Y, X) + \lambda L_{cyc}(G, F) \tag{4}$$

The structure of the generator network used in CycleGAN is shown in Figure 3a and consists of an encoder, a converter, and a decoder. The encoder contains three convolutional layers that extract the features of the source domain image. The converter has nine residual blocks that increase the depth and width of the network. Finally, the decoder is composed of three deconvolutional layers that reconstruct the image by upsampling. The discriminator adopts the idea of PatchGAN [22]. It begins by extracting features from the input image using four convolution layers. Then the output of multiple patches (70×70 image blocks) is obtained by convolution with 1 output channel number to achieve the purpose of "discrimination". The network structure is shown in Figure 3b. The following modifications were made to the original network for application to the data in this study:

1. Since the source domain image and the target domain image used in this study are vastly dissimilar, the discriminator can easily distinguish between true and false images, making the network susceptible to training failure. To address this issue, the study reduces the sensitivity of the discriminator by reducing one layer of the convolutional layer.
2. The instance regularization (IN) [27] in the original network is changed to batch regularization (BN) [28]. BN regularizes the same channel of all images in a batch, while IN only regularizes a single channel of a single image.

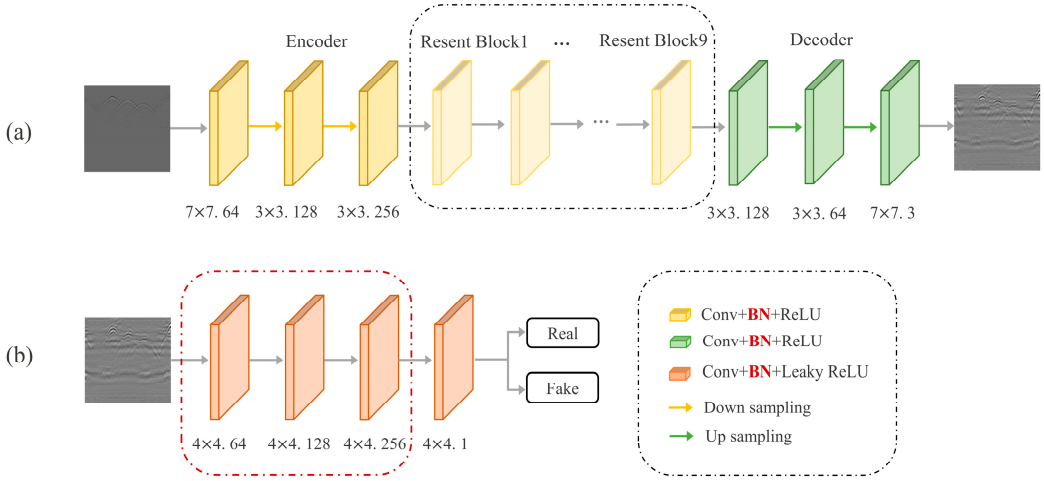


Figure 3. (**a**) Generator network structure. (**b**) Discriminator network structure.

2.1.2. YOLOv4-HPD

YOLOv4-HPD is a network used to extract the location and diameter parameters of the root target based on YOLOv4-Hyperbola [29], as shown in Figure 4. The network structure of YOLOv4-HPD follows YOLOv4- Hyperbola and is mainly divided into Input, BackBone, Neck, and Prediction. The backbone network is a convolutional neural network that aggregates and forms image features at different image granularities, using the CSP-Darknet53 [30,31]. The neck part is a series of network layers that mix and combine image features and pass image features to the prediction layer. In this part, the path aggregation network (PANet) structure [32] is referenced and the spatial pyramid pooling (SPP) module [33] is added. The head predicts root features in GPR images and generates the bounding box and hyperbolic keypoints. The CIou_Loss [34] is used as its loss function for the bounding box regression, and the hyperbolic keypoint regression uses the Wing loss function [35].

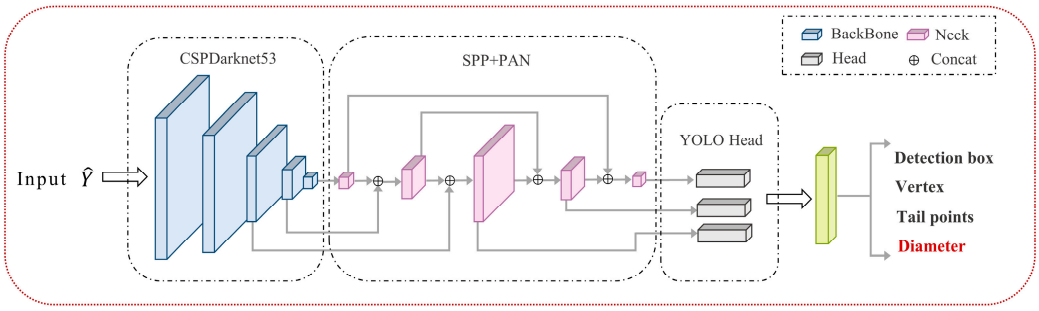


Figure 4. YOLOv4-HPD network structure.

The output dimension of YOLOv4-Hyperbola [29] is 16-D and contains bounding box coordinates, confidence, class, hyperbolic vertex, and four hyperbolic tail point coordinates. To obtain the location and diameter information of the root object simultaneously, it is necessary to further expand the prediction head and add the diameter prediction regression head. Therefore, we add a diameter prediction branch to YOLOv4-Hyperbola and redesign the loss function. The L1 loss function [36] has a stable gradient for each input value, and there is no gradient explosion problem. The solution is also robust and insensitive to outliers. Therefore, the diameter regression uses this loss function. The formula is shown in Equation (5). The output dimension of YOLOv4-HPD becomes 17-D, which includes the location information of the root (detection box, hyperbolic vertex, and four hyperbolic

tail points) and the attribute information of the root (diameter). The total loss function is defined as Equation (6).

$$loss_{dim} = \frac{1}{N}\sum_{i=1}^{N}|y_i - y_i'|, \quad (5)$$

$$loss = loss_{YOLOv4-Hyperbola} + \lambda_d \cdot loss_{\mathrm{dim}}, \quad (6)$$

where y_i is the predicted root diameter, y_i' is the true value of the root diameter, and λ_d is the weighting factor of the root diameter loss function.

Using the YOLOv4-HPD for recognizing and localizing root objects and estimating root diameter on GPR B-scan images can be divided into two stages: (I) preparing the input dataset and using the YOLOv4-Hyperbola model to label pseudo-target domain samples with key points to reduce the cost of manual labeling and to form labeled data after adding diameter information; (II) initializing the CNN model using the trained YOLOv4-Hyperbola model parameters, and then training and fine-tuning the YOLOv4-HPD using the training dataset for root localization and diameter estimation.

2.2. Data Description

2.2.1. Field Datasets

In the domain adaptation training process, the target domain data were derived from GPR images collected in two 30 m by 30 m plots in the field experiment. The plot experiments were conducted in the Xilinhot in Inner Mongolia (43°54′58″ N, 116°12′16″ E), China, in 2017 and 2018, respectively, and their specific locations are shown in Figure 5a.

Field validation data for root diameter were obtained from two sets of single-root burial control experiments. In the control experiments, a sand trench was first dug in a flat open area and holes were drilled in the vertical trench wall on one side of the trench, followed by the insertion of fresh root samples—of different diameters, relatively straight, and of the same length—of *Caragana microphylla* Lam. (*C. microphylla*) (as shown in Figure 5d). After insertion of the root samples, the portable GPR system probed along a pre-set measurement line at a horizontal angle of 90° to the root sample (Figure 5e). Control experiment 1 was located in the same area as the 30 m × 30 m sample experiment, and its profile pattern is shown in Figure 5b. Based on the angle between the root samples and the ground, control experiment 1 was divided into two groups: the first group of root samples was perpendicular to the horizontal ground and the second group of root samples was at an angle of 30° to the ground. Each group had two different sets of root samples. Four replicates in control experiment 1 were numbered A, B, C, and D. Table 1 summarizes information on the diameter of the root samples from each profile in control experiment 1. Control experiment 2 was conducted in 2012 at Plain and Bordered White Banner (42°37′31.4″ N, 114°45′27.5″ E), with 14 root samples in the profile shown in Figure 5c, and information on the root samples is listed in Table 2. The profile was numbered as profile E to validate the generalization of the method to measured data from different experimental sites. For the GPR images obtained for root detection in the field, the steps of data preprocessing include detrending, dewow filtering, background removal, and amplitude gain; these operations were conducted using MATGPR software [37].

Table 1. Diameter parameter of the selected root samples in control experiment 1.

θ	Depth (m)	Profile	Average Root Diameter (mm)						
			1	2	3	4	5	6	7
0°	0.3	A	9.68	14.73	15.02	13.22	10.84	Cavity	6.35
		B	7.71	8.73	10.82	13.13	15.40	17.91	Cavity
30°	0.2	C	Cavity	18.54	15.44	13.77	11.69	10.03	22.76
		D	8.11	10.03	11.26	13.68	15.46	22.76	Cavity

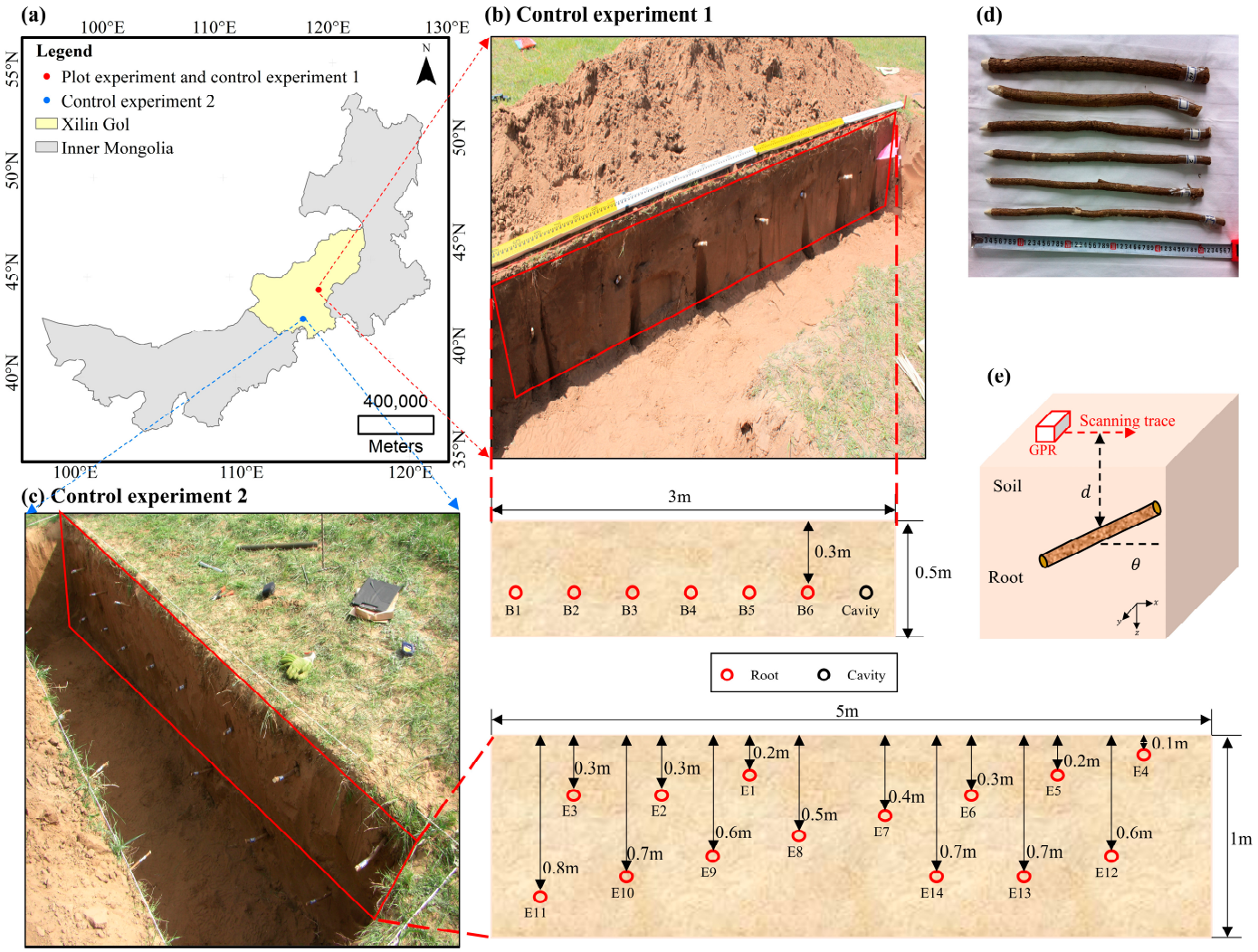


Figure 5. (**a**) The study site is located in Xilin Gol, Inner Mongolia, China. (**b**) Schematic of control experiment 1. (**c**) Schematic of control experiment 2. (**d**) Schematic of the root sample. (**e**) Schematic of the scan, with d and θ indicating depth and vertical inclination, respectively.

Table 2. Diameter parameter of the selected root samples of profile E in control experiment 2.

	1	2	3	4	5	6	7	8	9	10	11	12	13	14
Depth (m)	0.2	0.2	0.3	0.1	0.2	0.3	0.4	0.5	0.6	0.7	0.8	0.6	0.7	0.7
Average root diameter (mm)	13.06	15.46	14.49	13.54	16.65	17.56	15.53	19.66	18.31	19.72	20.05	13.4	16.08	13.79

2.2.2. Synthetic Datasets

GprMax V2.0 [10] was used to generate a simulated dataset of root samples with different diameters for training. In this experiment, the geometric domain size was set to 1.8 m × 0.5 m, and the center frequency of the GPR was set to 900 MHz, which is the same GPR frequency used in the field measurement experiments. The diameters of roots were set to 6 gradients: 10 mm, 14 mm, 18 mm, 22 mm, 26 mm, and 30 mm. Different dielectric constants of the root and soil correspond to different hyperbolic signals on the images. The experiment involved three groups of dielectric constants for roots (9.21, 12.01, and 14.81) and soil (3.70, 4.90, and 6.50), which were combined to produce nine sets of dielectric constant differences [38]. To enhance the model's ability to better learn the diameter features of the root object on the GPR image, the simulation scenarios are divided into two groups (as shown in Figure 6): Class I involves roots of the same diameter placed at different

horizontal positions and different depths, with variations in both soil and root dielectric constants, resulting in six sets of simulation data; Class II, on the other hand, involves roots of different diameters placed at varying horizontal positions and depths, with changes in both soil and root dielectric constants, resulting in two sets of simulation data. Each set simulated 450 images, and a total of 3600 simulated GPR root images with different attribute information were obtained as training data for the domain adaptation model.

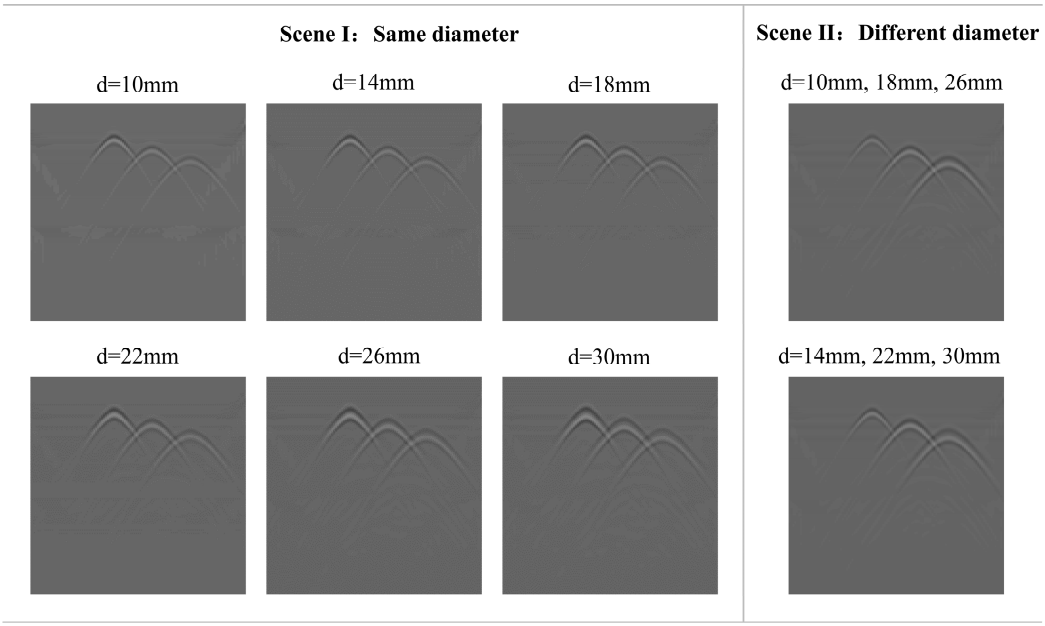


Figure 6. Examples of different root GPR images in two simulated scenarios.

2.3. Experimental Setup and Evaluation Metrics

The CMT-Net modeling experimental setup was divided into two parts, CycleGAN and YOLOv4-HPD. For CycleGAN, 3600 simulated GPR images (480 × 480) were obtained in the root diameter simulation experiment, to be used as the source-domain dataset, and 2418 actual GPR images (480 × 480) were cropped from the two 30m by 30m plots, to be used as the target-domain dataset. The source and target domain datasets were equally divided into training data and test data (1:1 ratio). The batch size was set to 2, the initial learning rate was set to 0.0002, and training was extended to more than 100 epochs.

In the second part of the experiment, 3600 simulated images were fed into the trained CycleGAN model, yielding 3600 generator-generated image samples. These images were then labeled with target boxes and keypoints using the YOLOv4-Hyperbola model [19]. The diameter value of each root object was added manually, and the resulting dataset was used as the YOLOv4-HPD input dataset. The data were divided into training (70%), validation (20%), and test (10%) datasets. The training dataset was used to optimize the parameters of the YOLOv4-HPD model, the validation dataset was used for model parameter tuning, and the test dataset was used to test the final performance of the model. The batch size was set to 6, the initial learning rate was set to 0.01, and a total of 200 epochs were trained. The PyTorch framework, a neural network framework open-sourced by Facebook, was adopted to train the YOLOv4-HPD model and CycleGAN model. The code is run on a server equipped with an Intel Core i9-10900K CPU of 3.7 GHz and an NVIDIA GeForce RTX 3080 GPU.

The performance of the YOLOv4-HPD model is evaluated by the following metrics: precision (Equation (7)), recall (Equation (8)), F1 (Equation (9)), $AP^{IoU=0.5}$, $AP^{oks=0.5}$, Absolute Error and Mean Absolute Error (MAE). AP (Average Precision) is the area between the precision–recall curve and the coordinate axis. $AP^{IoU=0.5}$ is the AP when the IoU

(Intersection over Union) = 0.5. Object Keypoint Similarity (*OKS*) [39] is a commonly used evaluation metric for keypoint detection algorithms. The *OKS* (Equation (10)) is analogous to the IoU. $AP^{oks=0.5}$ is calculated with the OKS threshold set to 0.5. The calculations are as follows:

$$Precision = \frac{TP}{TP + FP}, \tag{7}$$

$$Recall = \frac{TP}{TP + FN}, \tag{8}$$

$$F1 = 2 * \frac{Precision \cdot Recall}{Precision + Recall} \tag{9}$$

$$OKS = \frac{\sum_i (e^{-\frac{d_i^2}{2S^2\sigma_i^2}})\delta(v_i > 0)}{\sum_i \delta(v_i > 0)} \tag{10}$$

where *TP* is true positive, *FP* is false positive, and *FN* is false negative. v_i represents the visibility of the *i*-th keypoint; $\delta(*)$ indicates that if the condition $*$ holds, then $\delta(*) = 1$, otherwise, $\delta(*) = 0$. d_i represents the Euclidean distance between the true and predicted coordinates of the *i*-th keypoint; *S* represents the scale factor of the object, which is the square root of the area occupied by the object; σ_i is the normalization factor of the *i*-th keypoint.

3. Results

3.1. Domain Migration Results by CycleGAN

CycleGAN trained a total of 100 epochs. Different simulated images generated different real-world background images under different weight parameters. We used simulated data as much as possible to generate sample images similar to the real situation. Shown in Figure 7 are samples with different measured soil backgrounds generated by the trained CycleGAN model, corresponding to the two scenarios shown in Figure 6. The results show that the shape and opening size of the hyperbolic signal are well preserved and successfully converted to a soil background similar to the measured image. The brightness and texture of the images are greatly improved. It can be seen that the trained CycleGAN model can generate high-quality domain migration images that are highly similar to the measured data and can be used as training data.

3.2. Root Diameter Estimation by YOLOv4-HPD

The model was trained with 200 epochs, and tested on 360 images, comprising 270 images from scenario I and 90 images from scenario II. The trained YOLOv4-HPD model successfully localized all root objects on 360 test images while estimating the root diameter. The object detection evaluation indexes, including Precision, Recall, F1, and $AP^{IoU=0.5}$, all exceeded 95% on the test dataset. The keypoint evaluation index $AP^{oks=0.5}$ [29] has a value of 94.3% (see Table 3).

Figure 8 shows the detection results using YOLOv4-HPD on the test dataset, which mainly contains rectangular boxes with potential hyperbolic objects, five keypoints, and the extracted root diameter. Figure 8a–f show the images in simulated scenario I; Figure 8g,h show the images in simulated scenario II. Notably, YOLOv4-HPD accurately recognizes, locates, and extracts root diameters with errors of less than 2 mm for each object. The MAE of all root diameters in scenario I was between 1 mm and 2 mm (Figure 9). The largest MAE was observed for diameters of 10 mm, while the smallest was observed for diameters of 30 mm. In scenario II, the MAE ranged from 1 mm to 1.3 mm, with the highest estimated accuracy being 0.96 mm for diameters of 26 mm. Overall, the low error rate on the test dataset underscores YOLOv4-HPD's ability to accurately estimate root diameter parameters in diverse and complex environments.

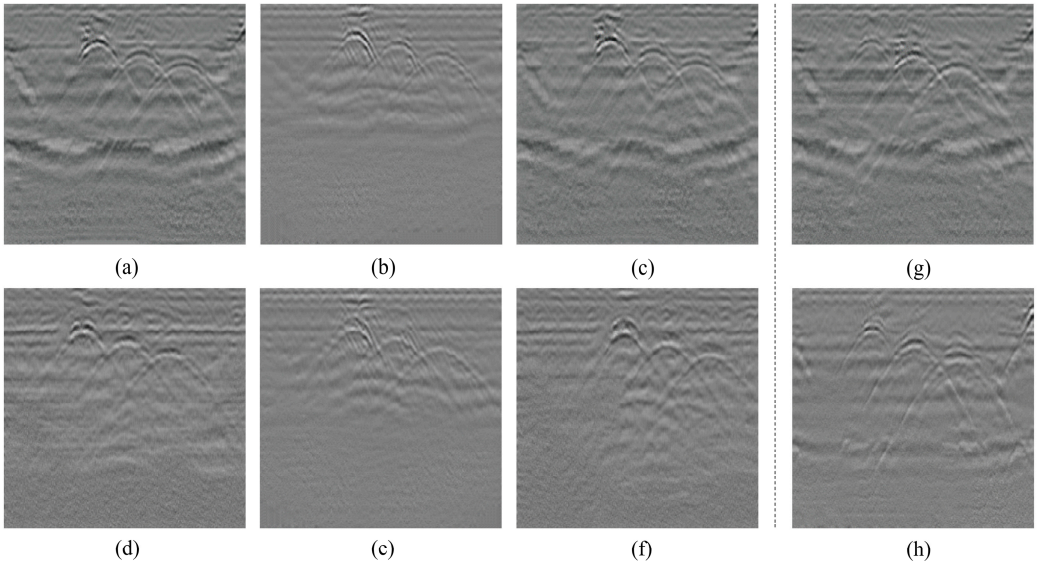


Figure 7. Example of domain migration results. (**a**–**f**) Domain migration results of scenario I. (**g**,**h**) Domain migration results of scenario II.

Table 3. Performance of the YOLOv4-hyperbola on the datasets of plot2.

Evaluation Indicators	Precision	Recall	F1	$AP^{IoU=0.5}$	$AP^{oks=0.5}$
Value of accuracy	99.8%	100.0%	99.9%	99.8%	94.3%

3.3. Model Generalization Verification

To verify the generalization performance of the model, the YOLOv4-HPD trained on the pseudo-target domain dataset ($\hat{Y}$) is applied to field-measured data. Figure 10 displays the results of root object localization and diameter estimation for five sand ditches. In the field experiment, 38 roots were measured, and the YOLOv4-HPD model recognized 30 roots from GPR images, achieving a root object identification rate of 80%.

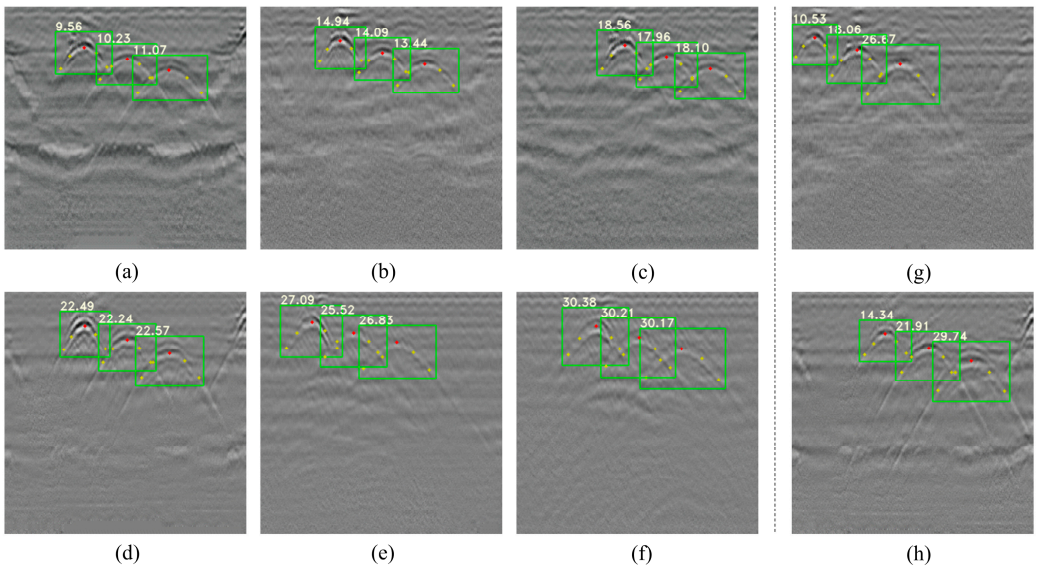


Figure 8. Root detection and root diameter estimation results of YOLOv4-HPD in CycleGAN domain migration results. The detected roots are enclosed in green boxes, and the corresponding root diameters are displayed in white text above the boxes. (**a**–**f**) Image detection results of scenario I. (**g**,**h**) Image detection results of scenario II.

Table 4 summarizes the real diameter, the predicted diameter, and the error between them of the root samples recognized on all images. Among the profiles, Profile A detected four root samples, all with absolute diameter estimation errors within 1 mm and a mean error of 0.56 mm. Profile B yielded six root signals, with absolute diameter errors ranging from 1.02 mm to 3.20 mm. Profile C detected four root signals, with varying diameter estimation errors, notably C4, with a large error. Profile D had five root signals, with relatively small errors for D2 and D6 but larger errors for others. Profile D exhibited the largest mean absolute error in root diameter estimation, at 5.07 mm. Profile E yielded eleven root signals, with absolute diameter errors ranging from 0.06 mm to 3.3 mm. The scatter plot (Figure 10f) shows that the majority of the samples are in close proximity to the 1:1 line, indicating a close match between the predicted and true values. The RMSE is only 2.83 mm. Although the root diameter estimation error was higher in measured data compared to simulation test data, the model remains effective on measured data despite not being trained on it.

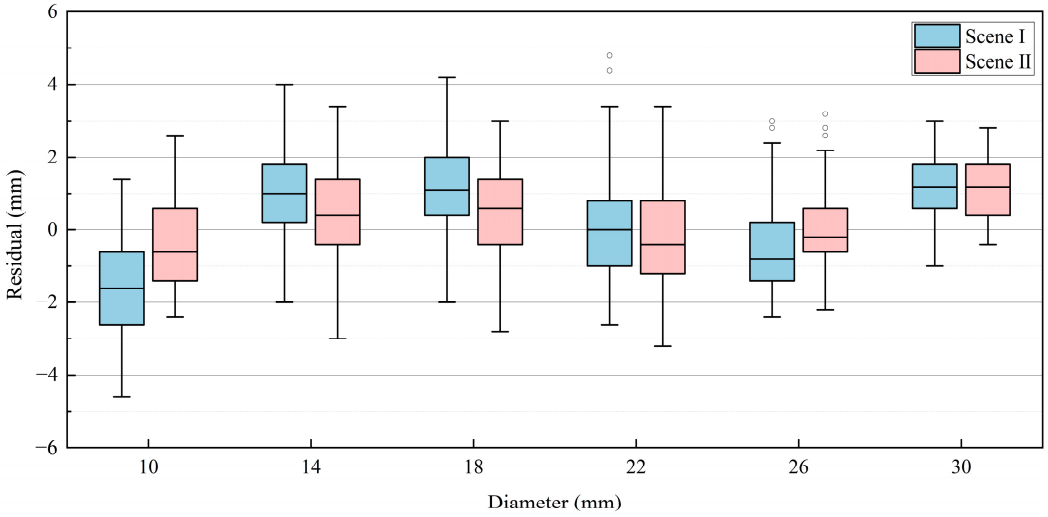


Figure 9. Boxplot of residuals distribution of two scenarios (the symbol "○" in the figure represents outlier).

Table 4. Predicted diameter and error statistics of YOLOv4-HPD in measured root samples.

Root	Diameter (mm)		Absolute Error (mm)	Relative Error (%)	MAE (mm)
	True Value	Prediction Value			
A2	14.73	14.45	0.28	1.90%	0.56
A3	15.02	15.12	0.10	0.67%	
A4	13.22	14.15	0.93	7.03%	
A5	10.84	11.78	0.94	8.67%	
B1	7.71	10.91	3.20	41.50%	2.12
B2	8.73	10.17	1.44	16.49%	
B3	10.82	13.99	3.17	29.30%	
B4	13.13	11.76	1.37	10.43%	
B5	15.40	14.38	1.02	6.62%	
B6	17.91	20.41	2.50	13.96%	
C2	18.54	17.88	0.66	3.56%	1.73
C3	15.44	14.05	1.39	9.00%	
C4	13.77	10.06	3.71	26.98%	
C5	11.69	10.54	1.15	9.84%	

Table 4. *Cont.*

Root	Diameter (mm)		Absolute Error (mm)	Relative Error (%)	MAE (mm)
	True Value	Prediction Value			
D2	10.03	11.53	1.50	14.96%	
D3	11.26	17.42	6.16	54.70%	
D4	13.68	19.08	5.40	39.47%	5.07
D5	15.46	23.92	8.46	54.72%	
D6	22.76	26.59	3.83	16.82%	
E1	13.06	11.80	1.26	9.65%	
E2	15.46	12.16	3.30	21.35%	
E3	14.49	13.60	0.89	6.14%	
E4	13.54	13.60	0.06	0.44%	
E5	16.65	17.00	0.35	2.10%	
E6	17.56	15.60	1.96	11.16%	1.47
E7	15.53	13.40	2.13	13.72%	
E8	19.66	18.40	1.26	6.41%	
E9	18.31	20.56	2.25	12.29%	
E11	20.05	17.88	2.17	10.82%	
E14	13.79	13.26	0.53	3.84%	

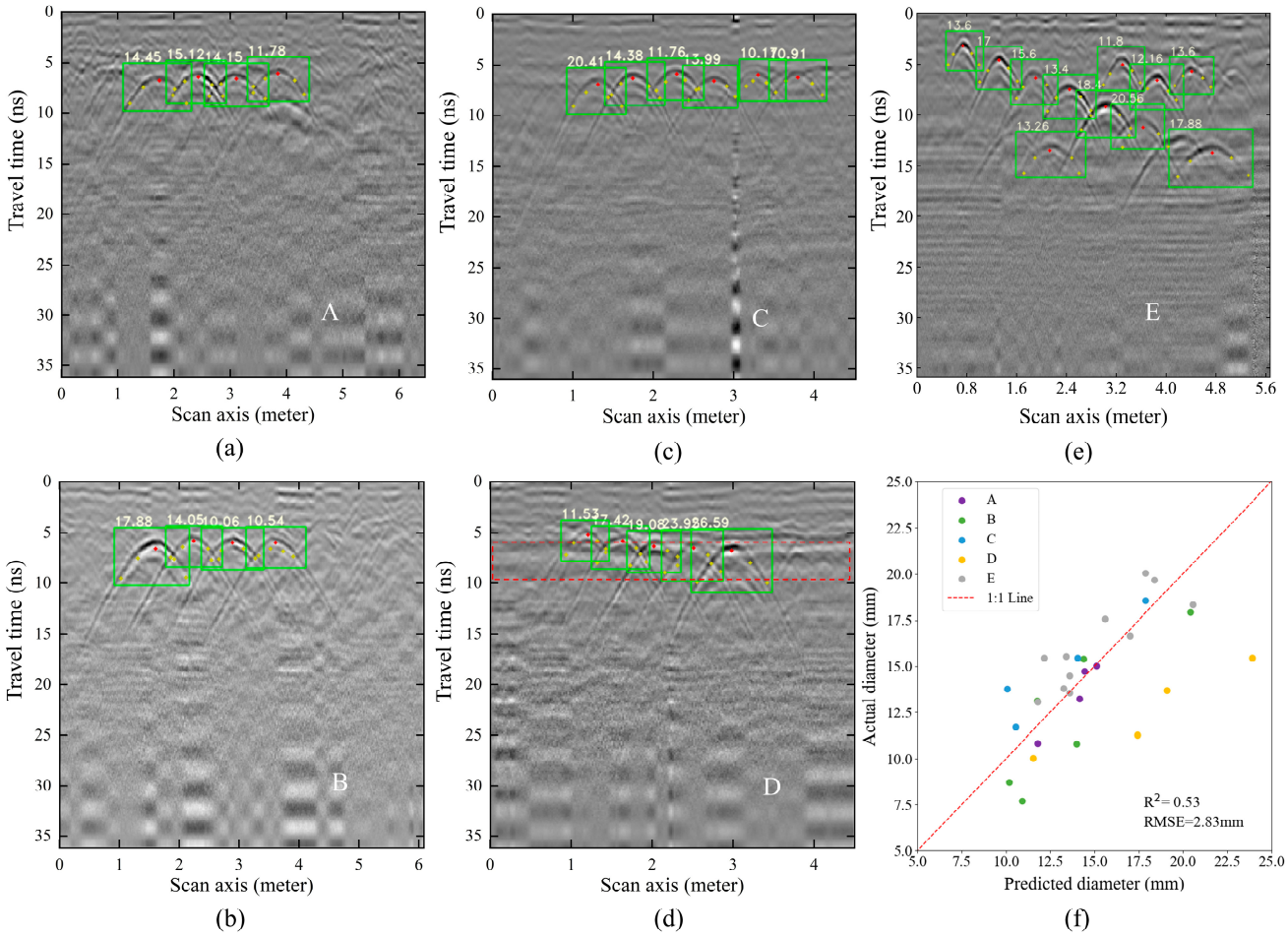


Figure 10. (**a**–**e**) are the detection results of YOLOv4-HPD on profiles A, B, C, D, and E, respectively. The detected roots are enclosed in green boxes, and the corresponding root diameters are displayed in white text above the boxes. (**f**) The relationship between the estimated diameter and the actual diameter of the measured root. The purple, green, blue, yellow, and grey dots represent root samples from each of the five trenches (A, B, C, D, and E) in the field experiment. The dotted line represents a 1:1 proportional line.

4. Discussion

4.1. Effectiveness of the Proposed CMT-Net Model

Obtaining accurate information on subsurface root diameters poses a significant challenge, hindering the construction of suitable training datasets for deep learning models. Consequently, deep learning models are more commonly employed for root object recognition rather than diameter estimation [24]. Root object recognition in existing studies is based on GPR B-Scan images [24,40], while root diameter estimation is mostly based on the selection of an A-Scan from the identified root signal [3,41]. Therefore, root identification and root diameter estimation are usually performed as separate processes. The proposed CMT-Net model effectively addresses these challenges. It allows simultaneous acquisition of root position and diameter from GPR B-Scan images, achieving fully automated end-to-end processing, which is crucial to facilitating the application of GPR in root quantification research.

The proposed CMT-Net model can be used to efficiently extract root diameter from GPR images for the following main reasons: (1) Simulation experiments encompassed root diameters ranging from 10 mm to 30 mm, aligning with the typical range of *C. microphylla* shrub root diameters in real-world environments [38]. (2) The diversity of simulated data was enhanced by incorporating nine combinations of soil and root dielectric constants, providing ample data variety for the CMT-Net model. (3) The CycleGAN network ensured invariant information of root reflection signal properties during training, facilitating the migration of real image domains to simulated images. This training approach, without requiring paired data, mitigated the difficulty of constructing the training dataset, which is a good basis for the subsequent application of the YOLOv4-HPD network to the measured data.

4.2. Comparison with Other Methods

Traditionally, the root diameter is estimated by constructing an empirical relationship between the root diameter and the amplitude or waveform parameters of the radar-reflected signal [41,42]. For example, Cui et al. (2011) utilized the time difference between the arrival of the electromagnetic wave at the bottom of the root and the arrival time at the top of the root (ΔT), which was manually extracted from the A-Scan data measured by GPR, as an independent variable, to build a linear regression model to estimate the root diameter [43]. The RMSE of the regression model on the validation data is 3.53 mm, whereas the RMSE of the root diameter extracted by the CMT-Net model is only 3.30 mm for the root samples in the field experiment (Figure 10f). Compared with the traditional method, the accuracy of the root diameter estimation has improved. In addition, the parameters used to estimate root diameter vary in different traditional methods and mostly rely on manual interpretation; thus, a unified operation procedure in data processing and parameter extraction is lacking; this needs to be further adjusted and examined in practical application. However, the CMT-Net model can overcome these problems.

So far, there are no publicly available datasets to compare the effectiveness of different deep learning algorithms in detecting root targets in GPR images. In the existing research, the MMI-Net neural network architecture proposed by Sun et al. can simultaneously estimate multiple parameters of the root system, including root depth, diameter, relative dielectric constant, and horizontal and vertical direction angles [17]. However, this model is only applicable to the measurement data of multi-polarized ground penetrating radar equipment, and many parameters need to be labeled in the training data. Therefore, it cannot be promoted for the single-polarized ground-penetrating radar equipment commonly used in the market. The research by Sun D. et al. requires two independent steps when estimating the root diameter [15]. First, YOLOv5s is used to identify the region of

interest (ROI) where the complete hyperbolic signal (signal reflected by root) is located, and then the hyperbolic shape in the region of interest (ROI) is extracted by image processing. Finally, the TPFC method is used to estimate the root diameter. They only used a deep learning algorithm (YOLOv5s) in the process of root detection. The TPFC method used to estimate the root diameter is similar to the traditional hyperbolic least squares fitting method. Moreover, the two processes are carried out separately, which weakens the advantages of the deep learning algorithm to a certain extent. Compared with these studies, the CMT-Net model we propose is applicable to GPR root image data of any polarization form. It can simultaneously identify and locate root targets and estimate the root diameter, thus achieving the effect of directly extracting the root diameter in an end-to-end manner. Future research can expand the model to estimate more root related parameters.

4.3. Potential Applications of CMT-Net

The CMT-Net model exhibits effectiveness in the acquisition of plant root spatial distribution and root diameter. This functionality substantially facilitates investigations into the physiological traits and growth mechanisms of plants, thereby enhancing our comprehension of plant adaptability across diverse environmental settings. Consequently, it holds certain potential in fields such as agriculture, forestry, and ecological environment monitoring. In agriculture, the CMT-Net model enables non-invasive detection and measurement of crop root positions. This empowers farmers to gain deeper insights into the health status of crop roots and identify the principal regions of water absorption. Subsequently, this knowledge can be harnessed to optimize irrigation and fertilization regimens, ultimately leading to improvements in crop yield and quality. In forestry, root system distribution and diameter are invaluable for deciphering the strategies employed by trees in water and nutrient acquisition. Such understanding is pivotal for the evaluation of forest health, thereby furnishing a foundation for forest management and conservation initiatives. In ecological environment monitoring, the CMT-Net model can be deployed for continuous monitoring of the root growth within ecosystems. This facilitates the assessment of the efficacy of ecological restoration projects and offers guidance for subsequent restoration work. Overall, the CMT-Net model is anticipated to introduce novel tools and methodologies for application in agriculture, forestry, and ecological environment monitoring.

4.4. Limitations and Future Outlook

While this study has shown promising results in locating root objects and estimating root diameter from GPR B-scan images, several limitations remain. Firstly, GPR, being a non-destructive geophysical detection technology, may miss detecting certain roots, such as taproots, due to hardware limitations and the complexity of subsurface environments [44]. This limitation can potentially hinder the model's performance.

Secondly, some field root samples yield unsatisfactory diameter prediction results. One potential reason is the sparse diameter gradient in the training data. The simulated diameter intervals were set at 4 mm, resulting in missing some sample data between intervals. This gap in the training data hampers the model's ability to capture the pattern of root diameter changes effectively, thus impacting its generalizability. Additionally, poor image quality caused by the inhomogeneity of water or organic matter content in underground soil can lead to noisy signals on GPR images. For example, in Figure 10d, it can be seen that the image (within the red dashed rectangular box) has a clear noise band, and the hyperbolic signals of the root reflections are exactly distributed in the noise band, which has little effect on the localization of the root target but affects the accuracy of the extraction of the root diameter. Despite the use of five profile data points for validation, more data are needed to support the use of this model across diverse scenarios and applications. Consequently,

researchers and practitioners are encouraged to undertake further validation of the model's effectiveness using additional measured data. This would facilitate more comprehensive support for its extension across diverse scenarios and applications.

To address these limitations, future studies should focus on refining methods and strategies for data simulation. Firstly, enhancing radar image resolution through the use of higher-frequency or multi-frequency fused GPR measurements could potentially improve accuracy. Secondly, considering the quality and coverage of simulated data and refining the diameter gradient to ensure the comprehensiveness and representativeness of the training data will improve the accuracy of the model in root diameter prediction. Finally, increasing the training data containing noise bands is essential to obtain more accurate diameter estimation results in complex measured environments.

5. Conclusions

This study focused on *C. microphylla* shrub roots, using a novel deep learning model, CMT-Net, for root object localization and diameter extraction from GPR B-Scan images. Measured data from a ground-coupled GPR system with a 900 MHz antenna and simulated data from GprMax V2.0 were utilized for model construction. CMT-Net's effectiveness was verified using both simulated and measured data. The total MAE of root samples across different diameters in simulated scenarios remained below 2 mm, ranging from 0.96 mm to 1.86 mm. Most root diameter estimation errors were within 2 mm. In measured data, hyperbolic signals from all root samples were accurately located, with 56% of root samples exhibiting absolute diameter errors within 2 mm and the smallest error recorded at 0.1 mm. The overall MAE for three sand trenches was within 2.20 mm, except for D. The RMSE of diameter estimation error for 19 measured root samples was 3.30 mm. These results affirm the CMT-Net model's capability in accurately locating root positions and estimating root diameter parameters in field experiments. This method provides a new idea for the estimation of other root attributes and facilitates the reconstruction of below-ground root system architecture.

Author Contributions: Conceptualization, X.C. (Xihong Cui) and M.S.; methodology, X.C. (Xin Cao) and X.C. (Xuehong Chen); supervision, L.G. and L.P.; writing—original draft preparation, S.L.; writing—review and editing, L.Z. and H.Y.; funding acquisition, X.C. (Xihong Cui). All authors have read and agreed to the published version of the manuscript.

Funding: This research was funded by the National Natural Science Foundation of China, grant number 42271329.

Data Availability Statement: Dataset available on request from the authors.

Acknowledgments: Thanks to the Chenlab team for helping with the experiments!

Conflicts of Interest: The authors declare no conflicts of interest.

References

1. Brunner, I.; Godbold, D.L. Tree Roots in a Changing World. *J. For. Res.* **2007**, *12*, 78–82. [CrossRef]
2. Gill, R.A.; Jackson, R.B. Global Patterns of Root Turnover for Terrestrial Ecosystems. *New Phytol.* **2000**, *147*, 13–31. [CrossRef]
3. Yamase, K.; Tanikawa, T.; Dannoura, M.; Ohashi, M.; Todo, C.; Ikeno, H.; Aono, K.; Hirano, Y. Ground-Penetrating Radar Estimates of Tree Root Diameter and Distribution under Field Conditions. *Trees* **2018**, *32*, 1657–1668. [CrossRef]
4. Metzner, R.; Eggert, A.; van Dusschoten, D.; Pflugfelder, D.; Gerth, S.; Schurr, U.; Uhlmann, N.; Jahnke, S. Direct Comparison of MRI and X-Ray CT Technologies for 3D Imaging of Root Systems in Soil: Potential and Challenges for Root Trait Quantification. *Plant Methods* **2015**, *11*, 17. [CrossRef] [PubMed]
5. Cui, X.; Guo, L.; Chen, J.; Chen, X.; Zhu, X. Estimating Tree-Root Biomass in Different Depths Using Ground-Penetrating Radar: Evidence from a Controlled Experiment. *IEEE Trans. Geosci. Remote Sens.* **2013**, *51*, 3410–3423. [CrossRef]

6. Nadezhdina, N.; Cermak, J. Instrumental Methods for Studies of Structure and Function of Root Systems of Large Trees. *J. Exp. Bot.* **2003**, *54*, 1511–1521. [CrossRef]
7. Norby, R.J.; Jackson, R.B. Root Dynamics and Global Change: Seeking an Ecosystem Perspective. *New Phytol.* **2000**, *147*, 3–12. [CrossRef]
8. Barton, C.V.M.; Montagu, K.D. Detection of Tree Roots and Determination of Root Diameters by Ground Penetrating Radar under Optimal Conditions. *Tree Physiol.* **2005**, *24*, 1323–1331. [CrossRef]
9. Jol, H.M. *Ground Penetrating Radar: Theory and Applications*, 1st ed.; Elsevier Science: Amsterdam, The Netherlands; Oxford, UK, 2009; ISBN 978-0-444-53348-7.
10. Giannopoulos, A. Modelling Ground Penetrating Radar by GprMax. *Constr. Build. Mater.* **2005**, *19*, 755–762. [CrossRef]
11. Chang, C.W.; Lin, C.H.; Lien, H.S. Measurement Radius of Reinforcing Steel Bar in Concrete Using Digital Image GPR. *Constr. Build. Mater.* **2009**, *23*, 1057–1063. [CrossRef]
12. Shihab, S.; Al-Nuaimy, W. Radius Estimation for Cylindrical Objects Detected by Ground Penetrating Radar. *Subsurf. Sens. Technol. Appl.* **2005**, *6*, 151–166. [CrossRef]
13. Muniappan, N.; Rao, E.P.; Hebsur, A.V.; Venkatachalam, G. Radius Estimation of Buried Cylindrical Objects Using GPR—A Case Study. In Proceedings of the 2012 14th International Conference on Ground Penetrating Radar (GPR), Shanghai, China, 4–8 June 2012; pp. 789–794.
14. Ristic, A.V.; Petrovacki, D.; Govedarica, M. A New Method to Simultaneously Estimate the Radius of a Cylindrical Object and the Wave Propagation Velocity from GPR Data. *Comput. Geosci.* **2009**, *35*, 1620–1630. [CrossRef]
15. Sun, D.; Jiang, F.; Wu, H.; Liu, S.; Luo, P.; Zhao, Z. Root Location and Root Diameter Estimation of Trees Based on Deep Learning and Ground-Penetrating Radar. *Agronomy* **2023**, *13*, 344. [CrossRef]
16. Dolgiy, A.; Dolgiy, A.; Zolotarev, V. Optimal Radius Estimation for Subsurface Pipes Detected by Ground Penetrating Radar. In Proceedings of the International Conference on Ground Penetrating Radar, Columbus, OH, USA, 19–22 June 2006.
17. Sun, H.-H.; Lee, Y.H.; Dai, Q.; Li, C.; Ow, G.; Yusof, M.L.M.; Yucel, A.C. Estimating Parameters of the Tree Root in Heterogeneous Soil Environments via Mask-Guided Multi-Polarimetric Integration Neural Network. *IEEE Trans. Geosci. Remote Sens.* **2022**, *60*, 5108716. [CrossRef]
18. Liang, H.; Fan, G.; Li, Y.; Zhao, Y. Theoretical Development of Plant Root Diameter Estimation Based on GprMax Data and Neural Network Modelling. *Forests* **2021**, *12*, 615. [CrossRef]
19. Saito, K.; Ushiku, Y.; Harada, T. Asymmetric Tri-Training for Unsupervised Domain Adaptation. *arXiv* **2017**, arXiv:1702.08400.
20. Morerio, P.; Cavazza, J.; Murino, V. Minimal-Entropy Correlation Alignment for Unsupervised Deep Domain Adaptation. *arXiv* **2017**, arXiv:1711.10288.
21. Shu, Y.; Cao, Z.; Long, M.; Wang, J. Transferable Curriculum for Weakly-Supervised Domain Adaptation. In Proceedings of the AAAI Conference on Artificial Intelligence, Honolulu, HI, USA, 27 January–1 February 2019; Volume 33, pp. 4951–4958.
22. Zhu, J.-Y.; Park, T.; Isola, P.; Efros, A.A. Unpaired Image-to-Image Translation Using Cycle-Consistent Adversarial Networks. In Proceedings of the 2017 IEEE International Conference on Computer Vision (ICCV), Venice, Italy, 22–29 October 2017; pp. 2242–2251.
23. Giannakis, I.; Giannopoulos, A.; Warren, C. A Machine Learning Scheme for Estimating the Diameter of Reinforcing Bars Using Ground Penetrating Radar. *IEEE Geosci. Remote Sens. Lett.* **2021**, *18*, 461–465. [CrossRef]
24. Hou, F.; Lei, W.; Li, S.; Xi, J. Deep Learning-Based Subsurface Target Detection from GPR Scans. *IEEE Sens. J.* **2021**, *21*, 8161–8171. [CrossRef]
25. Pham, M.-T.; Lefèvre, S. Buried Object Detection from B-Scan Ground Penetrating Radar Data Using Faster-RCNN. In Proceedings of the IGARSS 2018—2018 IEEE International Geoscience and Remote Sensing Symposium, Valencia, Spain, 22–27 July 2018; pp. 6804–6807.
26. Isola, P.; Zhu, J.-Y.; Zhou, T.; Efros, A.A. Image-to-Image Translation with Conditional Adversarial Networks. In Proceedings of the 2017 IEEE Conference on Computer Vision and Pattern Recognition (CVPR), Honolulu, HI, USA, 21–26 July 2017; pp. 5967–5976.
27. Song, Y. Instance Normalization: The Missing Ingredient for Fast Stylization. *arXiv* **2017**, arXiv:1607.08022.
28. Ioffe, S.; Szegedy, C. Batch Normalization: Accelerating Deep Network Training by Reducing Internal Covariate Shift. In Proceedings of the 32nd International Conference on Machine Learning, PMLR, Lille, France, 6–11 June 2015; pp. 448–456.
29. Li, S.; Cui, X.; Guo, L.; Zhang, L.; Chen, X.; Cao, X. Enhanced Automatic Root Recognition and Localization in GPR Images through a YOLOv4-Based Deep Learning Approach. *IEEE Trans. Geosci. Remote Sens.* **2022**, *60*, 5114314. [CrossRef]
30. Bochkovskiy, A.; Wang, C.-Y.; Liao, H. YOLOv4: Optimal Speed and Accuracy of Object Detection. *arXiv* **2020**, arXiv:2004.10934.
31. Wang, C.-Y.; Mark Liao, H.-Y.; Wu, Y.-H.; Chen, P.-Y.; Hsieh, J.-W.; Yeh, I.-H. CSPNet: A New Backbone That Can Enhance Learning Capability of CNN. In Proceedings of the 2020 IEEE/CVF Conference on Computer Vision and Pattern Recognition Workshops (CVPRW), Seattle, WA, USA, 14–19 June 2020; pp. 1571–1580.

32. Liu, S.; Qi, L.; Qin, H.; Shi, J.; Jia, J. Path Aggregation Network for Instance Segmentation. In Proceedings of the 2018 IEEE/CVF Conference on Computer Vision and Pattern Recognition, Salt Lake City, UT, USA, 18–23 June 2018; pp. 8759–8768.
33. He, K.; Zhang, X.; Ren, S.; Sun, J. Spatial Pyramid Pooling in Deep Convolutional Networks for Visual Recognition. *IEEE Trans. Pattern Anal. Mach. Intell.* **2015**, *37*, 1904–1916. [CrossRef] [PubMed]
34. Zheng, Z.; Wang, P.; Liu, W.; Li, J.; Ye, R.; Ren, D. Distance-IoU Loss: Faster and Better Learning for Bounding Box Regression. *AAAI* **2020**, *34*, 12993–13000. [CrossRef]
35. Feng, Z.-H.; Kittler, J.; Awais, M.; Huber, P.; Wu, X.-J. Wing Loss for Robust Facial Landmark Localisation with Convolutional Neural Networks. In Proceedings of the 2018 IEEE/CVF Conference on Computer Vision and Pattern Recognition, Salt Lake City, UT, USA, 18–22 June 2018; pp. 2235–2245.
36. Zhao, H.; Gallo, O.; Frosio, I.; Kautz, J. Loss Functions for Image Restoration With Neural Networks. *IEEE Trans. Comput. Imaging* **2017**, *3*, 47–57. [CrossRef]
37. Tzanis, A. matGPR Release 2: A Freeware MATLAB® Package for the Analysis & Interpretation of Common and Single Offset GPR Data. *FastTimes* **2010**, *15*, 17–43.
38. Liu, X.; Cui, X.; Guo, L.; Chen, J.; Li, W.; Yang, D.; Cao, X.; Chen, X.; Liu, Q.; Lin, H. Non-Invasive Estimation of Root Zone Soil Moisture from Coarse Root Reflections in Ground-Penetrating Radar Images. *Plant Soil* **2019**, *436*, 623–639. [CrossRef]
39. Cao, Z.; Hidalgo, G.; Simon, T.; Wei, S.-E.; Sheikh, Y. OpenPose: Realtime Multi-Person 2D Pose Estimation Using Part Affinity Fields. *IEEE Trans. Pattern Anal. Mach. Intell.* **2021**, *43*, 172–186. [CrossRef]
40. Lei, W.; Hou, F.; Xi, J.; Tan, Q.; Xu, M.; Jiang, X.; Liu, G.; Gu, Q. Automatic Hyperbola Detection and Fitting in GPR B-Scan Image. *Autom. Constr.* **2019**, *106*, 102839. [CrossRef]
41. Dannoura, M.; Hirano, Y.; Igarashi, T.; Ishii, M.; Aono, K.; Yamase, K.; Kanazawa, Y. Detection of *Cryptomeria japonica* Roots with Ground Penetrating Radar. *Plant Biosyst.* **2008**, *142*, 375–380. [CrossRef]
42. Zhu, S.; Huang, C.; Su, Y.; Sato, M. 3D Ground Penetrating Radar to Detect Tree Roots and Estimate Root Biomass in the Field. *Remote Sens.* **2014**, *6*, 5754–5773. [CrossRef]
43. Cui, X.; Chen, J.; Shen, J.; Cao, X.; Chen, X.; Zhu, X. Modeling Tree Root Diameter and Biomass by Ground-Penetrating Radar. *Sci. China Earth Sci.* **2011**, *54*, 711–719. [CrossRef]
44. Butnor, J.R.; Samuelson, L.J.; Stokes, T.A.; Johnsen, K.H.; Anderson, P.H.; González-Benecke, C.A. Surface-Based GPR Underestimates below-Stump Root Biomass. *Plant Soil* **2016**, *402*, 47–62. [CrossRef]

Disclaimer/Publisher's Note: The statements, opinions and data contained in all publications are solely those of the individual author(s) and contributor(s) and not of MDPI and/or the editor(s). MDPI and/or the editor(s) disclaim responsibility for any injury to people or property resulting from any ideas, methods, instructions or products referred to in the content.